30th Congress of the International Council
of the Aeronautical Sciences
DCC, Daejeon, Korea ; September 25-30, 2016

APPLICATIONS OF DISPLACEMENT TRANSFER FUNCTIONS TO DEFORMED SHAPE PREDICTIONS OF THE G-III SWEPT-WING STRUCTURE

Shun-Fat Lung[1] and William L. Ko[2]
[1]Jacobs Engineering Corporation, Edwards, California, 93523-0273
[2]NASA Armstrong Flight Research Center, Edwards, California, 93523-0723

Keywords: *shape, sensing, strain, displacement, DTFs*

PATENT PROTECTION NOTICE

The method for structure deformed shape predictions using Ko Displacement Theory for transforming surface strains into structural deformed shapes described in this Conference Paper is protected under *Method for Real-Time Structure Shape-Sensing*, U.S. Patent No. 7,520,176 issued April 21, 2009. Therefore, those interested in using the Method should contact NASA Innovative Partnership Program Office, NASA Armstrong Flight Research Center, Edwards, California for more information.

Abstract

In support of the Adaptive Compliant Trailing Edge [ACTE] project at the NASA Armstrong Flight Research Center, displacement transfer functions were applied to the swept wing of a Gulfstream G-III airplane (Gulfstream Aerospace Corporation, Savannah, Georgia) to obtain deformed shape predictions. Four strain-sensing lines (two on the lower surface, two on the upper surface) were used to calculate the deformed shape of the G III wing under bending and torsion. There being an insufficient number of surface strain sensors, the existing G III wing box finite element model was used to generate simulated surface strains for input to the displacement transfer functions. The resulting predicted deflections have good correlation with the finite-element generated deflections as well as the measured deflections from the ground load calibration test. The convergence study showed that the displacement prediction error at the G III wing tip can be reduced by increasing the number of strain stations (for each strain-sensing line) down to a minimum error of l.6 percent at 17 strain stations; using more than 17 strain stations yielded no benefit because the error slightly increased to 1.9% when 32 strain stations were used.

Nomenclature

ACTE	Adaptive Compliant Trailing Edge
AFRC	Armstrong Flight Research Center
DTF	displacement transfer functions
FEM	finite element model
G-III	Gulfstream III airplane
LRT	linear resistance transducer
NASA	National Aeronautics and Space Administration
P	bending load
T	torsion load
c_i	lower depth factor (vertical distance from neutral axis to lower surface strain station *i*, inches
$\bar{c}_i$	upper depth factor (vertical distance from neutral axis to upper surface strain station *i*, inches
d_i	strain-sensing line separation distance at strain-sensing station *i*
d_0	value of d_i at the wing root, $x = x_0 = 0$
d_n	value of d_i at the wing tip, $x = x_n = l$
h_i	(beam) depth of structure at strain station i
i	= 0,1,2, …,*n*, strain station identification number
l	length of strain-sensing line, inches
n	index for the last span-wise strain station (or number of strain-sensing domains)
w_n	wing tip chord length (width), inches
w_0	wing root chord length (width), inches
x, y	Cartesian coordinates (*x* in span-wise direction, *y* in lateral direction), inches
x_i	axial coordinate associated with i-th strain station, inches
y_i	deflection at axial location $x = x_i$, inches
ε_i	lower surface strain at $x = x_i$
$\bar{\varepsilon}_i$	upper surface strain at $x = x_i$
$(\Delta l)_i$	$\equiv (x_i - x_{i-1})$, domain length (distance between two adjacent strain stations at $x = x_{i-1}$ and $x = x_i$, inches
θ_i	slope of neutral axis at $x = x_i$, rad or deg
$(\,)'$	quantity associated with rear strain-sensing lines
ϕ_i	twist angle at $x = x_i$, rad or deg

1 Introduction

In late 2009, the NASA Armstrong Flight Research Center [AFRC] acquired a Gulfstream III [G-III] business jet airplane (Gulfstream Aerospace Corporation, Savannah, Georgia) to conduct various research projects. The G-III airplane, tail number 804, shown in Fig. 1, was modified and instrumented by NASA AFRC personnel to serve as a SubsoniC Research Aircraft Testbed [SCRAT] [1] for a variety of flight research experiments in support of the Environmentally Responsible Aviation [ERA] projects. The twin-turbofan engines provide long-term capability for efficient testing of subsonic flight experiments for NASA, the United States Air Force, other government agencies, academia, and private industry.

The current AFRC project utilizing the G-III airplane is the Adaptive Compliant Trailing Edge [ACTE] flap experiment. These unconventional adaptive compliant flap structures developed by FlexSys Inc. (Ann Arbor, Michigan) replaced the conventional Fowler flaps. Due to differences between the ACTE structure and the original Fowler flaps with respect to weight, geometry, and flight-testing conditions, the aerodynamic and inertial loads were expected to be different.

In order to protect the wing structure during flight, load equations were developed using strains loads data from a ground load calibration test. [2] These load equations were integrated in the Mission Control Room for real-time monitoring of the aerodynamic loads during flight. Wing deflected shape under load was also characterized and used to tune existing finite element models [FEMs] of the G-III wing structure.

Real-time deformed shape estimation of aerospace structures in flight is important for aircraft performance, safety of flight, and fuel efficiency. In order to enable the real-time shape sensing, Ko, et al. [3, 4, 5] developed the displacement transfer functions [DTFs] using a discretization approach to piecewise integrate the beam curvature-strain differential equations for transforming the in-flight measured surface strains into overall wing deformed shapes.

The DTFs combined with the on-board strain-sensing system (conventional strain gages or fiber optic sensors) thus form a powerful structure-shape-sensing technology invented by Ko and Richards [6] for in-flight deformed shape monitoring of flexible wings and tails. In addition, the real-time wing shape can be input to the aircraft control system for aeroelastic wing shape control. The accuracies of the DTFs were validated in the past using unswept aircraft wings, such as those found on the Ikhana Predator B (General Atomics, San Diego, California, USA) [7] and the Global Observer high-altitude, long-endurance remotely operated aircraft (AeroVironment, Inc., Simi Valley, California, USA). [8]

The objective of the present study is to apply the DTFs to the shape predictions of the G-III swept wing to demonstrate the accuracy and efficiency of the DTFs for a real-time deflection shape estimate tool. Unlike the unswept wings of the Ikhana and the Global Observer, the G-III swept wing is of more complicated geometry and has uneven strain distribution on the top and bottom surface skins. There being an insufficient number of surface strain sensors (strain gages are only installed on two spanwise locations for flight-test monitoring purposes), the existing G-III wing box FEM was used to generate surface strains for input to the DTFs. The resulting predicted deflections were then compared with the FEM-generated deflections as well as the measured deflections from the ground load calibration test for validating the accuracy of the DTFs when applied to the swept-wing case.

2 Displacement Transfer Functions

The G-III ground load calibration test and finite-element generated strains data can be used to examine the shape-prediction accuracy of the DTFs, and to reinforce the confidence in the DTFs for future aircraft wing deformed shape predictions.

The basic idea for the formulation of the DTFs [2, 3] is to discretize the slender structure cross section (embedded beam) along the surface strain-sensing line (span-wisely oriented) into *n* number of domains with domain junctures matching the strain stations at $x = x_i$ $(i = 1,2,3,\cdots,n)$ along the strain-sensing line. Thus, the surface strain distribution can be represented with piece-wise linear or piece-wise nonlinear functions in terms of surface strains at x_i. The discretization approach enables integrations of the embedded beam curvature-strain equation over each to yield slope and deflection equations in recursive forms. Due to the complexity of the structure geometry, various slope and deflection equations were developed based on non-uniform, slightly uniform, and uniform geometry of the structure. A typical set of slope and deflection equations written in recursive forms for non-uniform structures are shown, respectively, as Eq. (1) and Eq. (2):

Slope equation:

$$tan\theta_i = (\Delta l)_i \left[\frac{\varepsilon_{i-1} - \varepsilon_i}{c_{i-1} - c_i} + \frac{\varepsilon_{i-1}c_i - \varepsilon_i c_{i-1}}{(c_{i-1} - c_i)^2} log \frac{c_i}{c_{i-1}}\right] + tan\theta_{i-1}$$

$$\frac{Slightly\ nonuniform}{(c_{i-1} \approx c_i)} \rightarrow \frac{(\Delta l)_i}{2c_{i-1}}\left[\left(2 - \frac{c_i}{c_{i-1}}\right)\varepsilon_{i-1} + \varepsilon_i\right] + tan\theta_{i-1} \qquad (1)$$

$$\frac{Uniform}{(c_{i-1} = c_i = c)} \rightarrow \frac{(\Delta l)_i}{2c}(\varepsilon_{i-1} + \varepsilon_i) + tan\theta_{i-1}$$

$$(i = 1,2,3,\cdots,n)$$

Deflection equation:

$$y_i = (\Delta l)_i^2 \left[\frac{\varepsilon_{i-1}-\varepsilon_i}{2(c_{i-1}-c_i)} - \frac{\varepsilon_{i-1}c_i-\varepsilon_i c_{i-1}}{(c_{i-1}-c_i)^3}\left(c_i log \frac{c_i}{c_{i-1}} + (c_{i-1} - c_i)\right)\right] + y_{i-1} + (\Delta l)_i tan\theta_{i-1}$$

$$\frac{Slightly\ nonuniform}{(c_{i-1} \approx c_i)} \rightarrow \frac{(\Delta l)_i^2}{6c_{i-1}}\left[\left(3 - \frac{c_i}{c_{i-1}}\right)\varepsilon_{i-1} + \varepsilon_i\right] + y_{i-1} + (\Delta l)_i tan\theta_{i-1} \qquad (2)$$

$$\frac{Uniform}{(c_{i-1} = c_i = c)} \rightarrow \frac{(\Delta l)_i^2}{6c}(2\varepsilon_{i-1} + \varepsilon_i) + y_{i-1} + (\Delta l)_i tan\theta_{i-1}$$

$$(i = 1,2,3,\cdots,n)$$

Equations {(1), (2)} are DTFs for transforming surface strains into out-of-plane deflections for mapping out overall structure deformed shapes. The first set of equations {(1), (2)} (for non-uniform structures) was used in the deformed shape analysis of the wing of the G-III airplane.

2.1 Characteristics of Displacement Transfer Functions

In the DTFs, the deflections y_i $(i = 1,2,3,\cdots,n)(y_0 = 0)$ at axial location $x = x_i$ $(i = 1,2,3,\cdots,n)$ are expressed in terms of the inboard depth factors $(c_0, c_1, c_2, \cdots, c_i)$, and the associated inboard surface strains $(\varepsilon_0, \varepsilon_1, \varepsilon_2, \cdots, \varepsilon_i)$, including the values of $\{c_i, \varepsilon_i\}$ at $x = x_i$ where deflections y_i, are calculated.

It is important to mention that the DTFs are purely geometrical relationships, containing no material properties; however, it must be understood that the outputs of the surface strains e_i can be affected by material properties and internal structural configurations. When using the DTFs for shape predictions of complex structures such as aircraft wings, it is not necessary to know the material properties, nor the complex geometries of the internal structures.

2.2 Determination of Neutral Axis

For the calculations of deflection y_i of the G-III swept wing under bending load P and torsion load T, four strain-sensing lines (two on the lower surface and two on the upper surface), as shown in Fig. 2, are required because the depth factors are unknown. For pure bending, if the depth factors are known, only two sensing lines on the lower surface (or on the upper surface) are enough to sense both bending and torsion.

The unknown front and rear depth factors $[\{c_i, \bar{c}_i\}, \{c_i', \bar{c}_i'\}]$ can be calculated by using the associated pairs of lower and upper surface strains $[\{\varepsilon_i, \bar{\varepsilon}_i\}, \{\varepsilon_i', \bar{\varepsilon}_i'\}]$ at the same cross section $x = x_i$ as shown in Equations (3[a]) and (3[b]):

	Front strain-sensing cross section	Rear strain-sensing cross section	
Lower depth factors:	$c_i = \frac{\varepsilon_i}{\varepsilon_i + \bar{\varepsilon}_i} h_i$	$c_i' = \frac{\varepsilon_i'}{\varepsilon_i' + \bar{\varepsilon}_i'} h_i'$	(3[a])
Upper depth factors:	$\bar{c}_i = \frac{\bar{\varepsilon}_i}{\varepsilon_i + \bar{\varepsilon}_i} h_i$	$\bar{c}_i' = \frac{\bar{\varepsilon}_i'}{\varepsilon_i' + \bar{\varepsilon}_i'} h_i'$	(3[b])

in which $\{h_i(= c_i + \bar{c}_i), h_i'(= c_i' + \bar{c}_i')\}$ are, respectively, the depths at $x = x_i$ of structure cross sections along the front and rear strain-sensing lines (Fig. 2). For a linearly-tapered wing structure, $\{h_i, h'_i\}$ can be written as shown in Equation (3[c]):

$$h_i = h_0 - \frac{x_i}{l}(h_0 - h_n) \quad h'_i = h'_0 - \frac{x_i}{l}(h'_0 - h'_n) \qquad (3[c])$$

in which $[\{h_0, h'_0\}, \{h_n, h'_n\}]$ are, respectively, the values of $\{h_i, h'_i\}$ at the wing root $x = x_0$ and wing tip $x = x_i$.

2.3 Cross Sectional Twist Angle

If $\{y_i, y'_i\}$ respectively represent the deflections at axial location $x = x_i$ (Fig. 2) of the front and rear embedded beams separated by a distance d_i, then the cross sectional twist angle ϕ_i at $x = x_i$ can be calculated from Eq. (4):

$$\phi_i = sin^{-1}\left(\frac{y_i - y'_i}{d_i}\right) \quad ; \quad (i = 0,1,2,3,\cdots,n) \qquad (4)$$

3 Ground Load Calibration Test

The primary objective of the wing load calibration test was to establish an adequate database for developing load equations by applying a set of known loads and recording strain gage outputs. The equation coefficients were calculated by correlating the known applied loads with the strain gage output using linear regression techniques. These load equations were integrated in the Mission Control Room for real-time monitoring of structural strength limits. The collected wing deflection measurement, string potentiometer, and photogrammetry data were used to correlate with the FEM. The load calibration test as shown in Fig. 3 was performed in 2013 at the Flight Loads Laboratory (FLL) of AFRC. A total of 28 load cases using shot bags and hydraulic jacks were performed to achieve different shear, bending, and torsion combinations. A load cell is attached to each hydraulic jack to record the applied load and provide feedback to the load control system. For the wing deflection measurement, the jack linear resistant transducers [LRTs], string potentiometers, and photogrammetry were used to collect displacement data. Only string pot and LRT data were used for model correlation. Four extreme load cases were selected for the FEM correlation. These load cases are described in Table 1. The load pad and string pot locations are shown in Fig. 4 and Fig. 5, respectively.

4 Finite Element Model Correlation

In 2009, only a simplified finite element stick model of the G-III airplane was available for dynamic analysis. This model contained only beam elements for the modeling of wings. There was a need for a detailed FEM containing beam and plate elements for static load and stress analysis. The AFRC Aerostructures Branch decided to build a detailed FEM in-house in order to support the ACTE flight-testing research project.

The first G-III wing box FEM was created based on the G-III wing box computer-aided design [CAD] model. Due to the lack of material properties and skin thickness information, this model was tuned with experimental data using the MSC/NASTRAN (MSC Software Corporation, Newport Beach, California, USA) Solution 200 design optimization and sensitivity analysis procedure. Although this model correlated well with the experimental data after tuning, the thickness of each plate element may not have represented well the G-III wing skin thickness, and the strain calculation using this FEM may not be accurate.

In 2013 AFRC obtained the G-III wing stress report from Gulfstream. A second wing box FEM was then created based on the Gulfstream stress report. This stress report contained the nodal coordinates, skin thickness, and material properties information and was good enough to use to build a wing box FEM without further tuning of the model. Figure 6 shows the FEMs of the G-III wing. The correlation of the FEMs with the experimental data are shown in Tables 2, 3, 4, and 5. All deflections data shown in Tables 2 through 5 have been normalized for non-disclosure purposes. The large percentage errors shown in the tables are due to very small deflection at the inboard section of the wing. For load case 1, only string-pot-measured deflections were used to correlate with the FEM. For load cases 3 and 6, only the aft or forward side of the

LRT-measured deflections were used for finite element correlation, respectively. For load case 24, all of the LRT-measured deflections were used.

5 Displacement Transfer Functions Application

After correlation of the G-III wing box FEM, the strain output from the wing box FEM were entered into one of the DTFs for the wing deformed shape calculation. Since the second wing box FEM was created based on the information from the stress report, the thickness of the skin surface is more accurate than the first model. The second wing box FEM was thus used for the strain and deflection calculations.

Due to the non-uniform geometry of the G-III wing structure, four strain-sensing lines and non-uniform displacement transfer functions {Eqs. (1), (2)} were adapted to calculate the wing deformed shape. The four strain-sensing lines were located at the top and bottom surfaces of the front and rear spars. Each strain-sensing line contained 32 equally-spaced strain stations. The depth factors were calculated from the depth-factor equations {(3-a), (3-b)}.

Figures 7 and 8 depict finite-element-generated strain outputs from the front and rear strain-sensing lines for load case 24. The deflections calculated from the DTFs [using the bottom surface strains $\{\varepsilon_i, \varepsilon_i'\}$ and the lower depth factors $\{c_i, c_i'\}$], finite element method, and experiment are shown in Figs. 9 and 10. The deflections calculated from the DTFs compared very well with the finite-element- and LTRs-measured data.

Figure 11 shows the cross sectional twist angles calculated from Eq. (4) [in view of Equations (1) and (2)] and from finite element analysis. The twist angle is calculated based on the distance between the front and rear strain stations, as indicated in Fig. 6. The correlation between the finite element analysis and Eq. (4) is quite good.

A convergence study was also performed by using four different numbers (5, 9, 17, 32) of strain stations to study how the accuracy of the predicted deflections changes with the number of strain stations used. Results of the convergent study are shown in Fig. 12. It is shown that using more strain stations to calculate the deflection curve will match the finite-element deflection curve very well.

Figure 13 shows that the predicted wing-tip displacement error decreased with an increasing number of strain stations, reaching a minimum error of 1.6 percent at 17 strain stations. Increasing the number of strain stations beyond 17 yielded negligible benefit; the error gradually increased to 1.9 percent at 32 strain stations.

6 Concluding Remarks

The displacement transfer functions method for structure deformed shape predictions was applied to calculate the G-III swept-wing structure deformed shapes of a Gulfstream G-III airplane (Gulfstream Aerospace Corporation, Savannah, Georgia, USA). The non-uniform displacement transfer functions were used due to the non-uniform geometry of the G-III wing structure. Since the experimental surface strains data were not available, the surface strains generated by the correlated finite element model were used to enter into the displacement transfer functions for the deformed shape calculation. The calculated deformed shapes are very close to the correlated finite element results as well as to the measured data. The convergence study showed that using 17 strain stations, the wing-tip displacement prediction error was 1.6 percent, and that there is no need to use a large number of strain stations for G-III wing shape predictions.

References

[1] Baumann E, Hernandez J and Ruhf J. An Overview of NASA's SubsoniC Research Aircraft Testbed (SCRAT). AIAA-2013-5083, 2013.

[2] Lokos W, Miller E, Hudson L, Holguin A, Neufeld D and Haraguchi R. Strain Gage Loads Calibration Testing with Airbag Support for the Gulfstream III SubsoniC Research Aircraft Testbed (SCRAT). AIAA 2015 2020, 2015.

[3] Ko W, Richards W and Tran V. Displacement Theories for In-Flight Deformed Shape Predictions of Aerospace Structures. NASA/TP-2007-214612, 2007.

[4] Ko W and Fleischer V. Further Development of Ko Displacement Theory for Deformed Shape Predictions

of Nonuniform Aerospace Structures. NASA/TP-2009-214643, 2009.
[5] Ko W and Fleischer V. Methods for In-Flight Wing Shape Predictions of Highly Flexible Unmanned Aerial Vehicles: Formulation of Ko Displacement Theory. NASA/TP-2010-214656, 2010.
[6] Ko W and Richards W. Method for Real-Time Structure Shape-Sensing. U.S. Patent No. 7,520,176, issued April 21, 2009.
[7] Ko W, Richards W and Fleischer V. Applications of Ko Displacement Theory to the Deformed Shape Predictions of the Doubly Tapered Ikhana Wing. NASA/TP-2009-214652, 2009.
[8] Jutte C, Ko W, Stephens C, Bakalyar J, Richards W and Parker A. Deformed Shape Calculation of a Full-Scale Wing Using Fiber Optic Strain Data from a Ground Loads Test. NASA/TP-2011-215975, 2011.

7 Contact Author Email Address

mailto:Shun-Fat.Lung-1@nasa.gov

Copyright Statement

Tables

Table 1. Load cases description.

Load case	Type of loading	Maximum total load, lb	Description
1	Shot bags	-15,000	Outboard loading
3	Combined	22,500	Forward shot and aft hydraulic loading
6	Combined	22,500	Aft shot and forward hydraulic loading
24	Hydraulic	54,000	Maximum loading

Table 2. Finite element model correlations for load case 1.

String pot	Measured deflection	Wing box model 1		Wing box model 2	
		Deflection	Difference, %	Deflection	Difference, %
1	-1.00	-0.96	-4	-0.98	-2
2	-0.95	-0.91	-4	-0.93	-2
3	-0.44	-0.43	-3	-0.42	-5
4	-0.46	-0.45	-2	-0.44	-3
5	-0.23	-0.22	-4	-0.20	-11
6	-0.21	-0.20	-3	-0.19	-8

Table 3. Finite element model correlations for load case 3.

LRT	Measured deflection	Wing box model 1		Wing box model 2	
		Deflection	Difference, %	Deflection	Difference, %
1	1.00	0.99	-1	1.01	1
2		0.96			
3	0.83	0.82	0	0.83	0
4		0.80			
5	0.67	0.68	1	0.64	-4
6		0.65			
7	0.20	0.20	-3	0.15	-25
8		0.15			

Table 4. Finite element model correlations for load case 6.

LRT	Measured deflection	Wing box model 1		Wing box model 2	
		Deflection	Difference, %	Deflection	Difference, %
1		1.04			
2	1.00	1.03	3	1.07	7
3		0.86			
4	0.85	0.86	2	0.88	4
5		0.70			
6	0.67	0.71	5	0.68	1
7		0.18			
8	0.19	0.18	-9	0.16	-16

Table 5. Finite element model correlations for load case 24.

LRT	Measured deflection	Wing box model 1		Wing box model 2	
		Deflection	Difference, %	Deflection	Difference, %
1	1.00	1.07	7	1.09	9
2	1.00	1.05	5	1.07	7
3	0.86	0.90	4	0.90	5
4	0.86	0.89	3	0.89	4
5	0.70	0.74	6	0.70	1
6	0.70	0.73	4	0.69	-1
7	0.21	0.21	-2	0.17	-21
8	0.17	0.18	8	0.16	-2

Figures

Fig. 1. The G-III airplane, tail number 804.

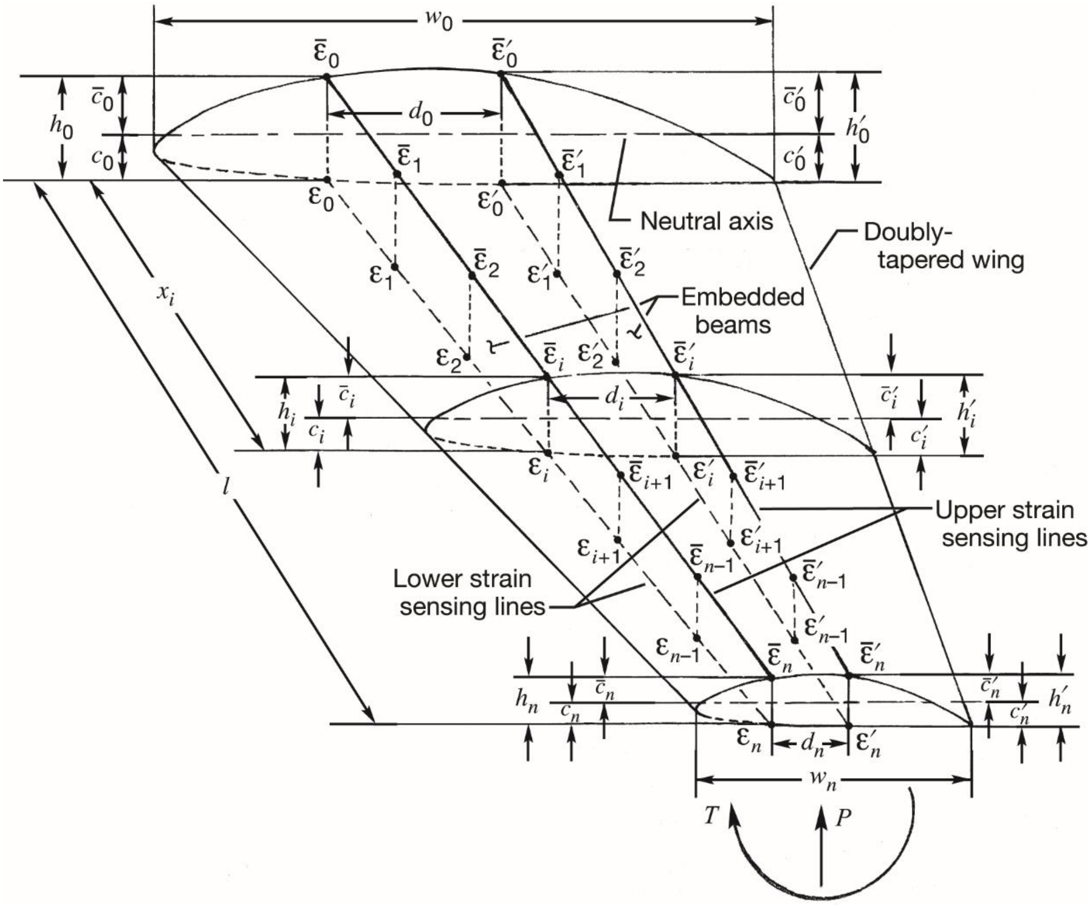

Fig. 2. Four-line strain-sensing system for deformed shape calculations of a wing structure under bending and torsion.

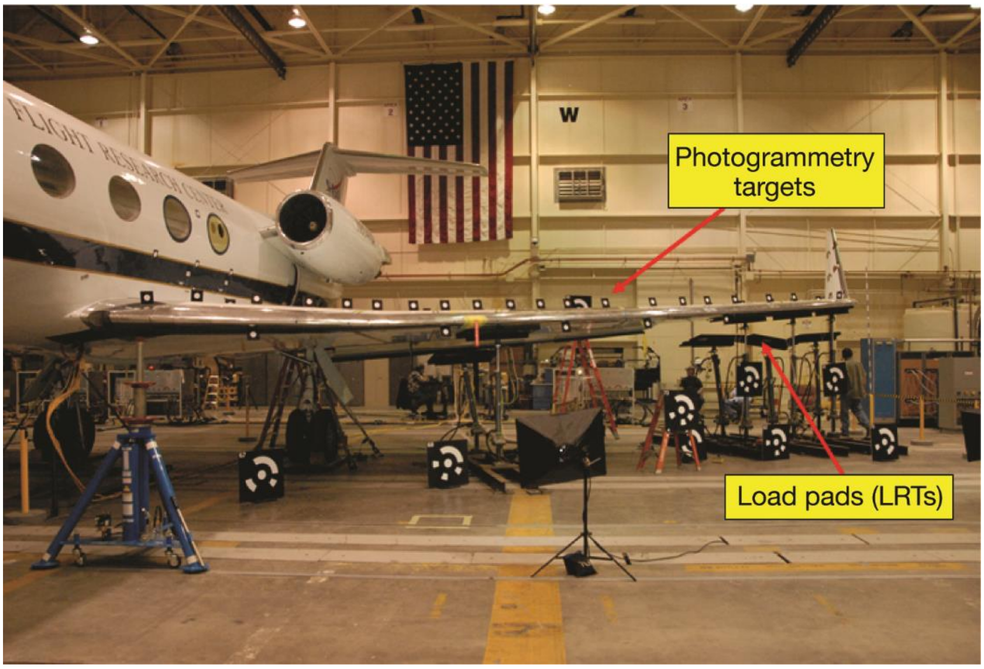

Fig. 3. The G-III wing load calibration test.

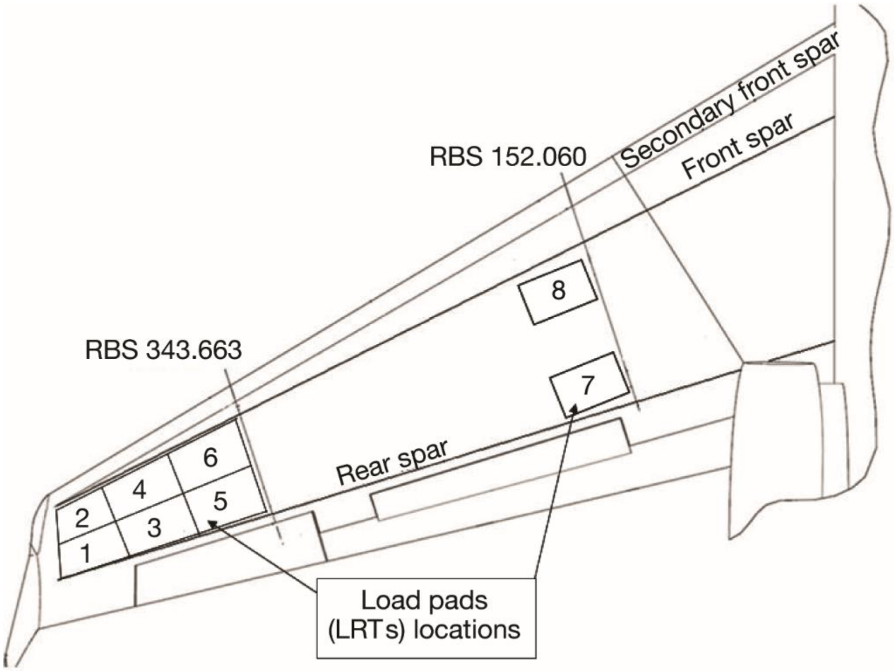

Fig. 4. Load pads (linear resistance transducers) layout.

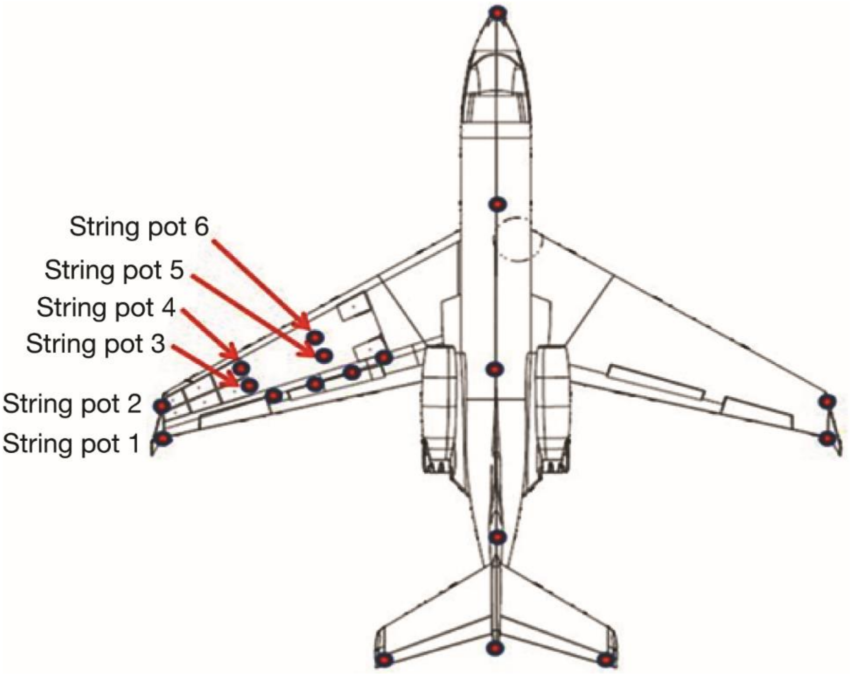

Fig. 5. String pots layout.

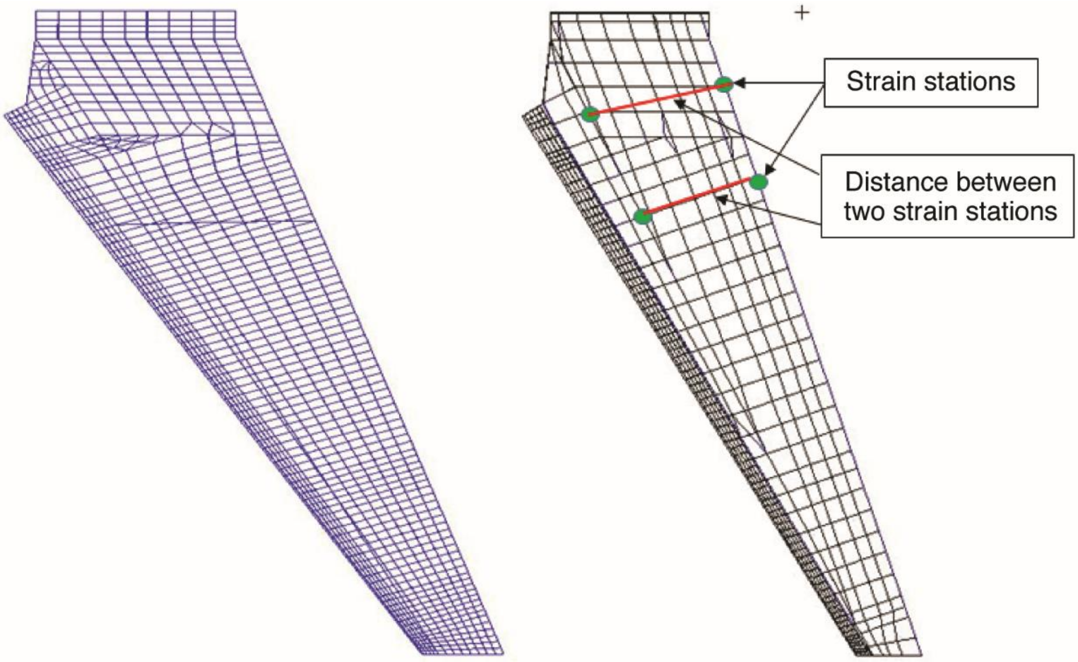

(a) First model (model 1).

(b) Second model (model 2).

Fig. 6. The G-III wing box finite element models.

Fig. 7. Strain from the rear strain lines.

Fig. 8. Strain from the front strain lines.

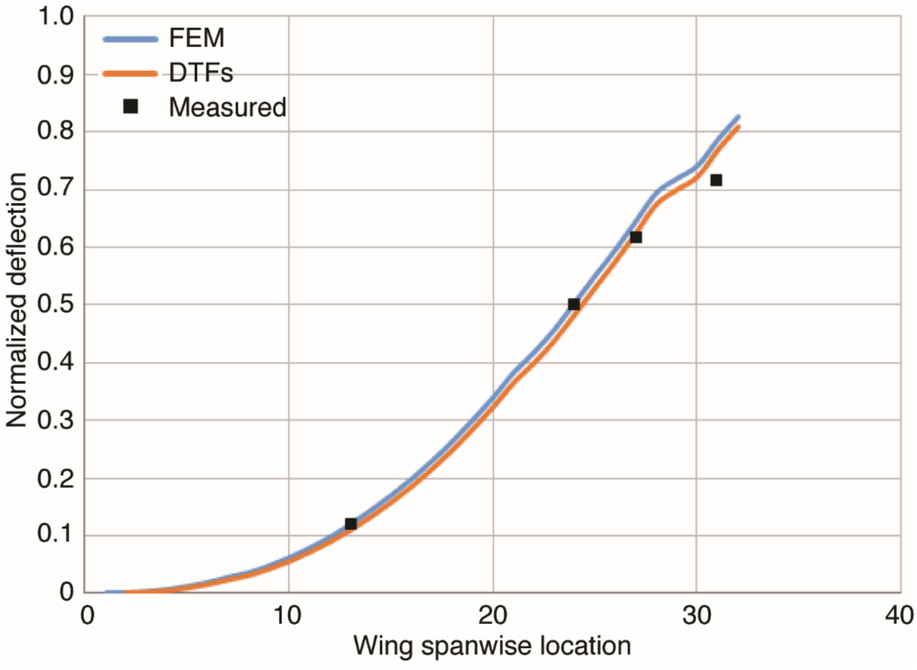

Fig. 9. Comparison of deflections along rear strain-sensing lines.

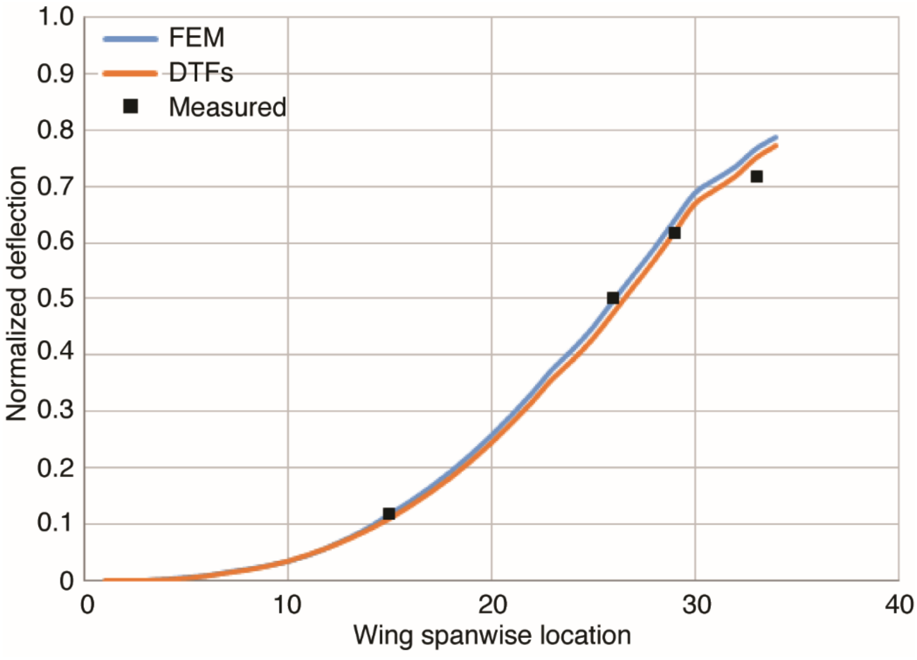

Fig. 10. Comparison of deflections along front strain-sensing lines.

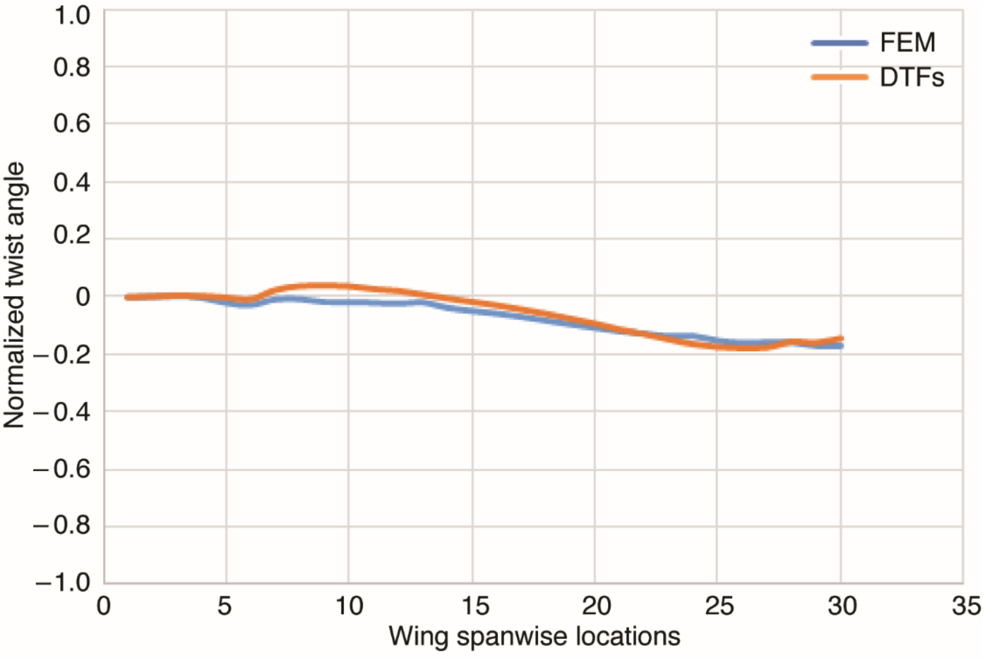

Fig. 11. Comparison of predicted and FEM-calculated cross sectional twist angles.

Fig. 12. Convergence of predicted deflection curves toward FEM deflection curve through increasing number of strain stations, *n*.

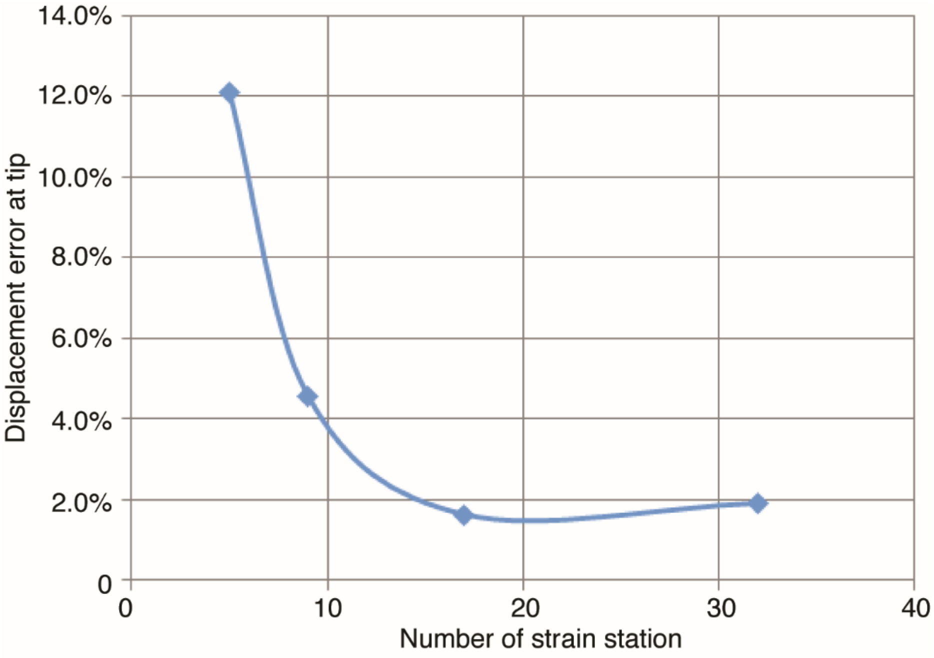

Fig. 13. Plot of deflection prediction error at wing tip as a function of the number of strain stations, *n*.